Catalysis Today 423 (2023) 114274

Contents lists available at ScienceDirect

Catalysis Today

journal homepage: www.elsevier.com/locate/cattod

Ruthenium incorporation into hydrotalcites-derived mixed oxides for phenol hydrogenation: Role of Mg/Al molar ratio

Isabel Barroso-Martín, Nadia Benmebirouk-Pareja, Maia Montaña, Juan Antonio Cecilia, Antonia Infantes-Molina *, Enrique Rodríguez-Castellón *

Department of Inorganic Chemistry, Crystallography and Mineralogy (Unidad Asociada al ICP-CSIC), Faculty of Sciences, University of Málaga, Campus de Teatinos, 29071 Málaga, Spain

ARTICLE INFO

Keywords:
Hydrotalcites
Mixed oxides
Ruthenium catalysts
Hydrogenation
Phenol

ABSTRACT

In this work the catalytic behaviour of Ru supported on mixed oxides derived from non-commercial hydrotalcites in phenol hydrogenation was studied in a batch reactor working at 30 bar and 200 °C. To this end, a set of catalysts with 2 wt% Ru and a Mg/Al molar ratio of 1, 2, 3 and 4 was synthesized. The catalysts were tested in phenol hydrogenation to assess the influence of Mg/Al ratio on the catalytic performance in terms of conversion and selectivities to cyclohexanol and cyclohexanone. Physicochemical characterization was performed by X-ray Diffraction (XRD), N_2 adsorption-desorption isotherms, dispersive X-ray spectroscopy in scanning transmission electron microscopy (EDS-STEM), CO chemisorption at 35 °C, CO_2 and NH_3 thermoprogrammed desorption (TPD) and X-ray Photoelectron Spectroscopy (XPS). The Mg/Al molar ratio employed determined the catalytic response of the resulting catalysts, obtaining the best catalytic performance (95.9 % conversion and 47.4 % cyclohexanone selectivity) with the sample with the lowest Mg/Al ratio, RuMA1. XRD results showed that in RuMA1 catalyst the hydrotalcite structure was completely transformed into the corresponding mixed oxide after thermal treatment and was also the only one in which $MgAl_2O_4$ spinel was not formed. In addition, RuMA1 presented the highest specific surface area, the greatest Ru dispersion, as evidenced by CO-chemisorption and EDX-STEM analysis, as well as a good balance between basic and acid sites and a greater proportion of Bronsted acid sites that also explain it greater selectivity to cyclohexanol.

1. Introduction

Cyclohexanone and cyclohexanol are high value-added products widely used in polymer and chemical industry as organic solvents in oil paints or varnishes [1] or as intermediates in nylon, oxalic acid and caprolactam and adipic acid syntheses [2]. Cyclohexanone can be obtained through several synthetic approaches, such as cyclohexene hydration [3], phenol hydrogenation [4,5] and cyclohexane oxidation [6]. The latter has been the most used one traditionally, giving as main product KA oil, which is a mix of cyclohexanone (K) and cyclohexanol (A) of which more than one million tons are annually produced by this procedure [7]. However, this process is energy intensive and yields to low selectivity and a wide range of by-products which are usually difficult to separate, which has motivated the search for more efficient synthetic approaches [8]. In this context, the phenol hydrogenation arises has a promising alternative for several reasons. On the one hand, this process presents greater atomic efficiency and can be carried out in one or two steps, as well as in gas or liquid phase, being the latter the preferred option in terms of cost savings [9–11]. On the other hand, phenol can be obtained from the degradation of biomass-derived lignin, which is a sustainable, and widespread carbon neutral precursor.

It has been reported that in phenol hydrogenation, hydrogen is added to the aromatic ring by a spillover mechanism. The spill-over process could be defined as the synergy between the sites with acid-base character and metal sites that promotes the surface migration of activated hydrogen from the metal site to acid-base sites, thus, spill-over is more likely to occur with the involved sites in close proximity and the adsorption configuration is strongly related to the number of acid and basic sites around the metal sites [3,12]. Reaction pathways reported for this reaction are depicted in Fig. 1 and state that phenol can be totally hydrogenated to cyclohexanone or partially hydrogenated to the enolic intermediate, cyclohexenol, which in turn can undergo either hydrogenation to form cyclohexanol or isomerization to cyclohexanone. Besides, cyclohexanone can be reduced to cyclohexanol [5].

* Corresponding authors.
E-mail addresses: ainfantes@uma.es (A. Infantes-Molina), castellon@uma.es (E. Rodríguez-Castellón).

https://doi.org/10.1016/j.cattod.2023.114274
Received 3 May 2023; Received in revised form 19 June 2023; Accepted 29 June 2023
Available online 30 June 2023

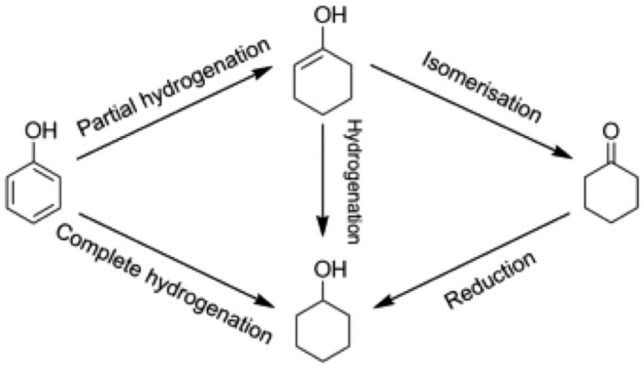

Fig. 1. Proposed reaction pathways for phenol hydrogenation [5].

Taking into consideration the importance of hydrogen activation in this reaction, noble metals like Pd or Ru are benchmark hydrogenating agents [4] given their outstanding ability not only to absorb hydrogen but also to activate it and promote hydrogen spill-over. However, the intrinsic high costs associated with these elements have promoted the development of catalysts' synthesis approaches that lower the metallic load used in the catalyst formulation without decreasing its activity and selectivity. Supporting the noble metal on a high specific surface area solid with certain acid-base and textural properties is one of the most used strategies in catalysis to attain catalysts with a high metallic dispersion and very low metal loading [13]. In addition, it is known that supports with acid-base properties and moderate specific surface area improve both thermal stability and metallic phase dispersion [14]. Regarding phenol hydrogenation, the reaction mechanism proposed by Neri et al. [15] suggests that basic sites could ease phenol chemisorption with a non-planar configuration, hindering the complete hydrogenation of phenol to cyclohexanol. Likewise, acid sites favour the isomerization of cyclohexenol to cyclohexanone and the strong interaction between the latter and the acid site inhibits further the hydrogenation to cyclohexanol [16,17].

Carbon supports have resulted more effective in phenol hydrogenation when acid-treated, demonstrating the importance of acid-base properties in this reaction. Li et al. [18] studied Pd supported on basic- and acid-treated carbon catalysts in the phenol hydrogenation at 10 bar and 100 °C in a stainless-steel autoclave, reporting a worsening in the catalytic activity after the basic treatment of the carbon support due to the formation of phenolate, which suppressed the reaction, and also in the cyclohexanone selectivity due to α-H abstraction in cyclohexanone as a consequence of the hydroxyl groups presence, which accelerate cyclohexanone's hydrogenation to cyclohexanol.

Metal oxides have also been tested as supports for phenol hydrogenation. In fact, Al_2O_3 is one of the most used supports for hydrotreating reactions, but its acidity leads to catalyst deactivation. The study carried out by Scirè et al. [19] using Pd supported on Al_2O_3, CeO_2 and La_2O_3 catalysts demonstrated a close relation between acidity and cyclohexanone selectivity, since acid-base properties have a strong influence on the adsorption-desorption equilibrium of reactants and products. Vono et al. [9] reported that titania enhances the activity and selectivity in Pd and Ru supported on titania-modified silica catalysts in phenol hydrogenation at 6 bar and 75 °C thanks to the weak acidity provided by titania that favours phenol interaction with the support and, hence, increases the selectivity to cyclohexanol.

Hydrotalcites have been thoroughly investigated as supports for noble metals thanks to their compositional and structural properties, like lamellar porous structure or tuneable metal composition [20–22]. The octahedral layers allow a uniform distribution of M^{2+} and M^{3+} cations, leaving the charge compensation anions in the intermediate layer that will eventually be removed during the thermal treatment in which the collapse of the lamellar structure occurs and highly dispersed mixed MgO and Al_2O_3 oxides are formed. When noble metals are incorporated, this collapse of the hydrotalcite structure can lead to a high dispersion of stable noble metal particles with close interaction with the support [23,24]. Moreover, the synthesis approaches are likely to influence the catalytic activity of the supported catalysts since the tuning of Mg and Al contents can modify the acid-base properties, which have a crucial role in catalysis. Narayanan and Krishna [25] studied the influence of calcination temperature and alumina content of hydrotalcites with Zn^{2+} and Li^{+} as brucite layer cations, reporting that Pd dispersion followed opposite trends. For calcination temperature over 450 °C, Pd dispersion decreased whereas it increased with alumina presence, but the latter also favoured catalyst deactivation. Calcination has also shown a strong effect on the acid-base properties of hydrotalcites, since at certain temperatures (400–600 °C) the formation of mixed metal oxides with an abundance of Lewis base sites is promoted [26]. Moreover, when calcined over 600 °C, acid sites contribution has been reported to be minimal due to sintering [27]. Besides, the M^{2+}/M^{3+} ratio used in the hydrotalcite formulation greatly influences the basicity. For example, in Mg/Al hydrotalcites, the highest relative concentration of strong, resistant basic sites is associated with MgO, while that of medium to weak basic sites is enhanced with higher Al content [28].

The use of mixed oxides derived from non-commercial hydrotalcites containing different Mg/Al molar ratio represents a novel and promising approach in the phenol hydrogenation, since the control of the acid-base properties through the synthesis strategy and the compositional flexibility in hydrotalcite-like materials offer challenging new opportunities for the development of active catalysts for phenol hydrogenation with high selectivity for high-value products such as cyclohexanone or cyclohexanol. In this context, mixed oxides derived from non-commercial hydrotalcites with different Mg/Al molar ratio and containing 2 wt% ruthenium were prepared and tested in the hydrogenation of phenol at 200 °C and 30 bar. The aim of this work is to shed light on the influence of Mg and Al content in the relationship between activity and both structure and acid-base properties of the prepared materials and provide insights on the development of efficient and selective catalysts for phenol hydrogenation for high added value products.

2. Experimental

2.1. Synthesis of the catalysts

Hydrotalcites with different Mg/Al molar ratios (1, 2, 3, 4) were prepared following a co-precipitation method by dropwise addition of 1 M NaOH and 0.25 M Na_2CO_3 mixture, as precipitating agent, to a solution containing the proper amounts of $Mg(NO_3)_2{\cdot}6H_2O$ and $Al(NO_3)_3{\cdot}9H_2O$) in deionized water. The amounts of these two chemicals were adjusted to obtain the desired Mg/Al molar ratios. The pH was maintained at 10 during the procedure. After precipitation, the obtained solid was recovered by filtration and washed several times with deionized water, dried at 120 °C for 24 h and calcined at 550 °C for 4 h. The hydrotalcites were denoted as MA1, MA2, MA3 and MA4, corresponding to the Mg/Al molar ratios of 1, 2, 3 and 4, respectively. Finally, the hydrotalcites were calcined at 550 °C for 2 h at a heating rate of 5 °C min^{-1} to obtain the corresponding mixed oxides.

Ruthenium was incorporated into the obtained mixed oxides following incipient wetness impregnation method, where well-known volumes of an aqueous $RuCl_3$ solution were added to the hydrotalcite-derived mixed oxides to obtain 2 wt% Ru supported catalysts. After drying at 120 °C for 24 h, the samples were calcined at 500 °C for 2 h (5 °C min^{-1}) and named RuMA1-c, RuMA2-c, RuMA3-c and RuMA4-c.

Prior to the catalytic test, the catalysts were reduced at 450 °C for 2 h at a heating rate of 5 °C min^{-1} and with an hydrogen flow of 60 mL min^{-1}. The reduced catalysts were named RuMA1-r, RuMA2-r, RuMA3-r y RuMA4-r. Lastly, the catalysts after reaction were identified as RuMA1-u, RuMA2-u, RuMA3-u y RuMA4-u.

2.2. Characterization techniques

XRD analysis were carried out in a PANalytical EMPYREAN diffractometer equipped with a rotating sample holder and an automatic loader. Measurements were registered using $CuK_{\alpha 1,2}$ (1.5406 Å) radiation, 45 kV and 40 mA with the sample rotating at 10 rpm during the measurements. The diffractograms were collected in the range of 4–80° of 2θ, with a step size of 0.0167°.

N_2 adsorption-desorption isotherms at − 196 °C were performed with an ASAP 2020 Micromeritics apparatus. Prior to N_2 adsorption, all samples were degasified at 200 °C and 2.7 MPa for 12 h.

CO chemisorption analyses were carried out at 35 °C in an ASAP 2020c Micromeritics equipment. Prior to CO chemisorption, the samples were reduced at 450 °C for one hour with a heating rate of 5 °C min^{-1}.

Thermoprogrammed CO_2 and NH_3 desorption (CO_2-TPD and NH_3-TPD) were performed in a AutoChem III apparatus from Micromeritics. Prior to the analysis, the samples were cleaned using flowing He at 500 °C and further reduced at 450 °C with a heating rate of 5 °C min^{-1} for 1 h. Afterwards, the samples were cooled up to 100 °C before saturation with CO_2 or NH_3.

XPS measurements were performed with a PHI 5700 spectrometer (Physical Electronics) with non-monochromatic MgKα radiation and equipped with a multichannel detector. Spectra were registered with PHI ACCESS ESCA-V 6.0F software and constant pass-energy mode at 29.35 eV.

High resolution TEM images were collected with a TALOS F200x, working at 200 kV and 5.5 A for TEM images. STEM analyses were performed with a HAAD detector working at 200 kV and 200 nA. Local composition analyses were carried out with an EDX Super-X system with four X-ray detectors and a X-FEG beam. Image J software was used for particle size measurements.

Collected reaction samples were analysed by gas chromatography in a Shimadzu GC-14B chromatograph equipped with a flame ionization detector and a TRB-14 capillary column.

2.3. Catalytic test

The hydrogenation of phenol was carried out in a batch reactor (PID&Tech and Iberfluid) with semi-automatic sample collection working at 30 bar, 200 °C and 800 rpm. The reaction medium consisted of 100 mL of 2 wt% phenol in decalin and 200 mg of powder reduced catalyst. Prior to reaction, the reaction system was purged with nitrogen. Liquid sample collection was carried out every hour for 5 h.

3. Results and discussion

3.1. Characterization results

In order to identify the crystalline phases present in the catalysts before and after reduction, high angle X-ray diffraction measurements were carried out. Fig. 2(a) displays diffractograms for calcined catalysts, where the characteristic diffraction peaks of the MgO periclase phase at 2θ = 44° and 63° (PDF no. 04-014-0288) were present in all samples. Moreover, the samples with a Mg/Al molar ratio higher than 1 showed the diffraction peaks of $MgAl_2O_4$ spinel phase at 2θ = 32°, 37°, 45° and 65° (PDF no. 01-084-0377) and those attributed to $Mg_{0.83}Al_{0.17}(CO_3)_{0.08}(OH)_2(H_2O)_{0.75}$ (PDF no. 04-015-1683) at 2θ = 11° and 22°, which is typical of hydrotalcite-like materials, indicating that the structure was not completely collapsed during the thermal treatment at higher Mg/Al ratios [29]. Diffractions peaks related to aluminium as Al_2O_3 were not detected, probably due to a high dispersion of this phase with low crystallinity together with the formation of the spinel phase. Besides, diffraction peaks associated to ruthenium(IV) oxide were present at 2θ = 28°, 35° and 54° (PDF no. 00-040-1290) whose particle size, calculated by using the Scherrer equation were 143.6, 81.9, 303.3 and 314.9 nm, for samples with a molar ratio of 1, 2, 3 and 4, respectively. With respect to reduced catalysts, the high angle diffractograms were registered and collected in Fig. 2(b). As expected after reduction, the RuO_2 diffraction peaks disappeared and a diffraction peak at 2θ = 43.8° is noticeable between the main diffraction signal of MgO at 2θ = 43.0° and the second diffraction peak of $MgAl_2O_4$ at 2θ = 44.8°, which is related to the (101) diffraction peak of hexagonal metallic Ru (PDF no. 03-065-7645). As for calcined samples, the MgO and $MgAl_2O_4$ diffraction peaks are well defined for Mg/Al ratios higher than 1. In the case of RuMA1-r sample, besides the Ru diffraction signal, only a broad diffraction peaks corresponding to MgO are present, i.e, for this sample the crystallinity of the phases formed was poor. No peaks related to non-collapsed hydrotalcites phases were found after reduction.

Textural parameters were assessed by N_2 adsorption-desorption isotherms at − 196 °C and displayed in Fig. 3 for calcined catalysts and the corresponding textural values in terms of BET surface area values and pore volume summed up in Table 1.

As observed, calcined catalysts presented type IV isotherms according to IUPAC classification (see Fig. 3) [30], characteristic of mesoporous materials. Adsorption at high relative pressures suggests the presence of wide mesopores as well as macroporosity, probably due to nitrogen filling in the interparticle space. When Mg content increased, a

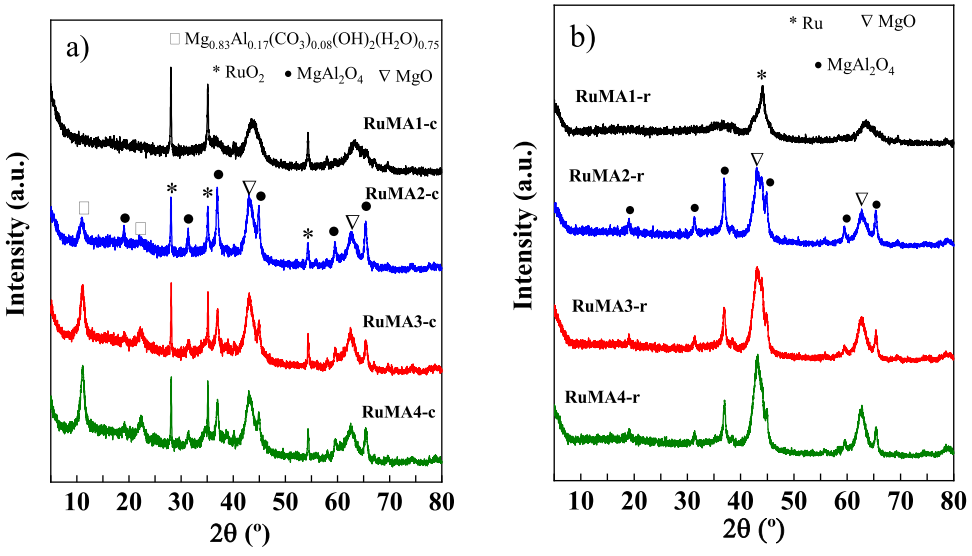

Fig. 2. High angle X-ray diffractograms for (a) calcined and (b) reduced catalysts.

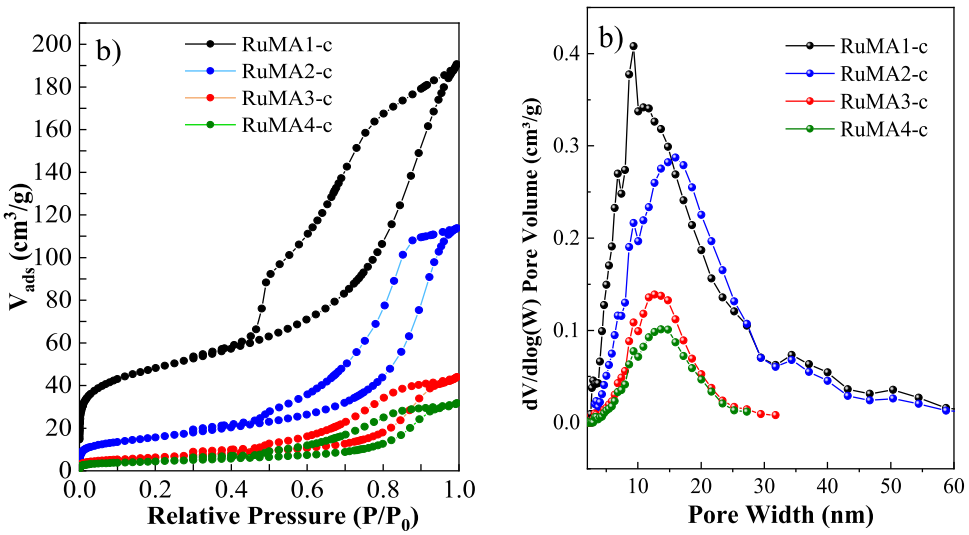

Fig. 3. N_2 adsorption-desorption isotherms (a) and pore size distribution (b) of calcined catalysts.

Table 1
Textural properties of calcined catalysts.

Sample	S_{BET} (m^2 g^{-1})	Pore volume (cm^3 g^{-1})	Pore size (nm)
RuMA1-c	170	0.27	11
RuMA2-c	55	0.16	17
RuMA3-c	22	0.06	14
RuMA4-c	16	0.05	16

decrease in the quantity of adsorbed nitrogen at these relative pressures was evidenced, suggesting a decrease in macroporosity for samples with Mg/Al > 1. Type H2(b) hysteresis loop due to capillary condensation is evidenced in all samples, indicating the existence of complex pores, as well as pore blockage. In fact, the minimal desorption at relative pressures between 1 and 0.7, together with the abrupted closure of the hysteresis loop (especially in samples with Mg/Al = 1) is typical of bottleneck-type materials [31]. It is worth mentioning that in RuMA1-c sample, the onset of the isotherm presented a sharp knee, which is indicative of a considerable contribution of microporosity.

Considering the textural values, which depend to a large extent on the Mg/Al ratio present, calcined catalysts suffered a decrease in these values at higher Mg/Al ratios, which has been previously reported and could be justified considering the larger atomic radius of Mg [32]. Pore width distribution (calculated using DFT method) in Fig. 3(b) showed a unimodal distribution, with average pore size of 15 nm (see Table 1). As expected, RuMA1-c presented the smallest average pore size, due to the greater contribution of microporosity in comparison with its counterparts.

The reducibility of Ru in the catalyst was evaluated by H_2-TPR and the registered curves are plotted in Fig. 4. It is observed that all samples were completely reduced at 450 °C therefore this was the reduction temperature used. Hydrogen consumption profiles presented two peaks: a relatively sharp, smaller one between 190 °C and 210 °C, associated with the reduction of RuO_x and RuO_2 segregated species [33]; and the main one at *ca.* 350 °C, attributed to strongly interacted ruthenium oxide species in the metal-support interface [34]. In the case of the RuMA1-c catalyst, the low-temperature signal is shifted to higher temperature (240 °C), and the proportion of this reduction peak is much higher than for the other three samples, and also indicating a better reducibility. The different behaviour in this sample is assigned to two important facts: a larger interaction with the non-spinel Mg-Al-containing species of the support that shifts the main reduction peak to higher temperatures; and the greater interaction of Ru with Mg species as previously observed in literature, favouring its reduction [34].

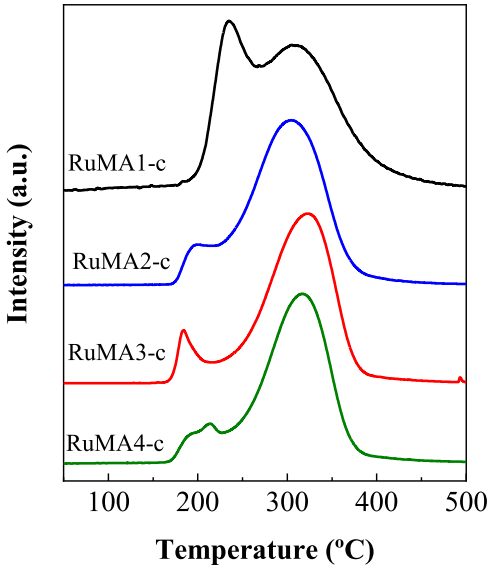

Fig. 4. H_2-TPR profiles of the calcined catalysts.

The distribution of ruthenium on the surface of reduced catalysts was evaluated from STEM coupled to EDX analysis and collected in Fig. 5. In all cases, a homogeneous distribution of Ru species was clearly observed regardless the Mg/Al ratio employed. Although some agglomerates were evidenced in some cases.

Further information about the exposed metallic surface and therefore the dispersion of metallic ruthenium was obtained from CO-chemisorption measurements and the results are included in Table 2. It can be clearly observed how the dispersion and the metallic surface decreased with the Mg/Al ratio, playing, as expected, an important role in ruthenium exposure. Again RuMA1-r sample shows the higher values.

Due to the importance of acid and basic sites in this type of reaction, thermoprogrammed desorption of probe molecules was carried out. In this sense, the basicity of the reduced catalyst was studied by means of CO_2 thermoprogrammed desorption and the registered curves plotted in Fig. 6(a). Besides, basicity values, standing for the total amount of adsorbed CO_2 per gram of catalyst and the normalized basicity, are collected in Table 2. According to Debecker et al. [28], the adsorption of CO_2 probe molecule could lead to the formation of monodentate, bidentate and bicarbonate anions, depending on whether the basic site is

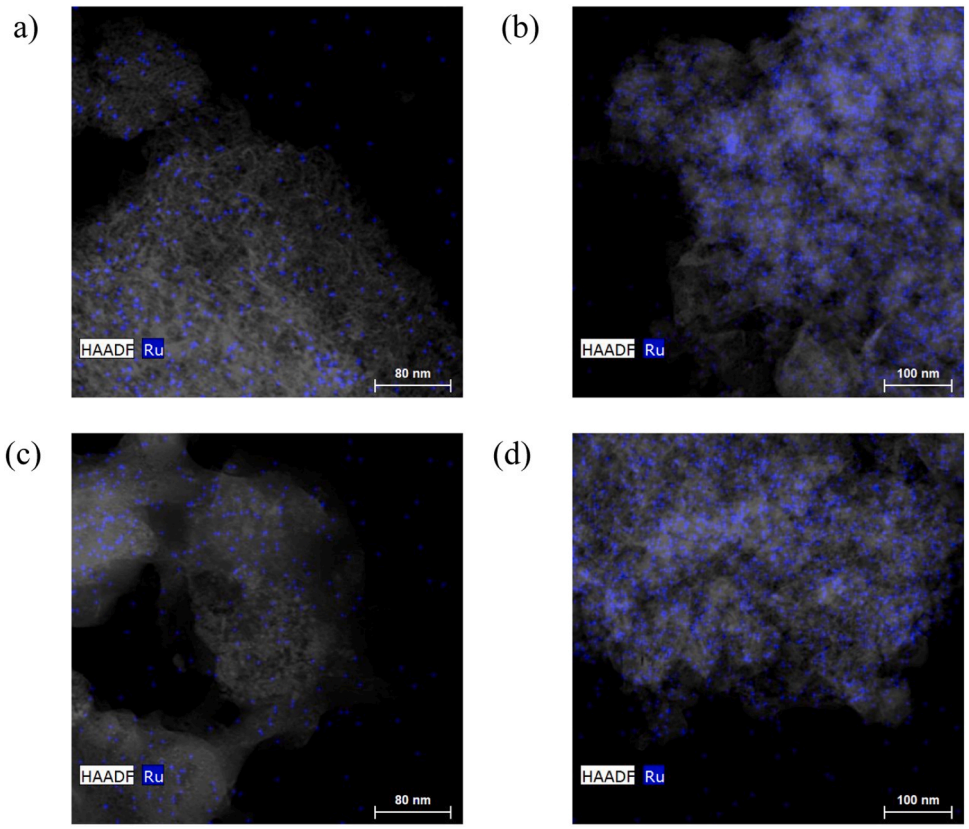

Fig. 5. EDX-STEM Ru mapping of (a) 2RuMA1-r, (b) 2RuMA2-r, (c) 2RuMA3-r and (d) 2RuMA4-r.

Table 2
Quantification of CO_2 and NH_3 TPD experiments and metallic information from CO chemisorption analyses.

Sample	μmol CO_2 g^{-1}	μmol CO_2 m^{-2}	μmol NH_3 g^{-1}	μmol NH_3 m^{-2}	Ru dispersion (%)	Metallic area (m^2 g^{-1})
RuMA1-r	134	0.79	575	3.4	6.0	0.44
RuMA2-r	96	1.75	382	6.9	3.9	0.29
RuMA3-r	89	4.05	379	17.2	3.4	0.25
RuMA4-r	79	4.94	318	19.9	3.3	0.24

strong, medium or weak, respectively. While monodentate carbonate anions are related to low-coordinated oxygen atoms, bidentate ones require acid-base pairs such as Al^{3+}-O^{2-} or Mg^{2+}-O^{2-} [35]. All samples presented a main desorption peak centred at *ca.* 160 °C, which indicates a weak nature basicity in these samples due to weakly basic hydroxyl groups [36]. Nonetheless, the broadness and slow decay of the peak suggest the coexistence of both weak and medium-strength basic sites, mainly from Mg^{2+}, as well as the contributions of hydroxyl and carbonate groups in the catalysts, as evidenced by XPS results. Although an increase in the amount of adsorbed CO_2 was expected with Mg content, the observed trend was the opposite due to the formation of $MgAl_2O_4$ spinel, as previously reported by other authors [37] and linked to the decrease in the surface area. In fact, if the normalized basicity is considered, the expected trend is observed: the greater the Mg amount, the higher the normalised basicity.

On the other hand, the acidity of reduced catalysts was assessed by means of ammonia thermoprogrammed desorption. Acidity values, as μmol NH_3 per gram of catalyst and normalized acidity as well, are collected in Table 2. The registered curves for NH_3 desorption are plotted in Fig. 6(b), in which an asymmetric, broad peak is observed for all samples, starting at 100 °C and with a maximum at 190–210 °C, indicating the mainly weak nature of the acid sites, although some contribution of medium strength acid sites is evidenced with ammonia desorption from 250 °C to 400 °C. Mg-Al hydrotalcite-derived materials contain both Brønsted and Lewis acid sites. The latter are attributed to Al-O-Mg species located inside de MgO structure in which Al^{3+} is preferentially located in octahedral sites, whereas Brønsted sites, weaker ones, are associated with surface proton [38], which suggests that the acidity of the samples mainly comes from Brønsted acid sites given their weak nature. Zhao et al. [39] reported that the desorption at low temperatures is attributed to hydrogen bond adsorption at Bronsted acid sites, while desorption at higher temperatures is attributed to coordination adsorption on Lewis acid sites. Moreover, the deconvolution of the desorption profiles indicates that Mg content diminished the contribution of the deconvoluted peak at lower temperature, from 60 % to 55 %, indicating that the lower the Mg/Al ratio employed, the higher the desorption at low temperatures and therefore the amount of Bronsted acid sites.

The acidity of the samples followed the same trend as the basicity, decreasing as the Mg content increased, which suggest that the availability of acid sites also decreases with the formation of the $MgAl_2O_4$ spinel and directly related with the surface area. In this regard, as observed for basicity, normalized acidity increased with Mg content. If basicity and acidity values are compared, acidity is significantly higher, as previously reported by other authors [38,40].

Finally, the surface chemical composition as well as oxidation states of the elements in the catalysts' formulation were studied by XPS analysis. The Al 2*s* core level spectrum was registered instead of the Al 2*p* due to an Auger signal of Mg overlapping. Likewise, considering that the Ru 3*d* spectrum overlaps with the main signal associated with the adventitious carbon at 248.8 eV, Ru 3*p* signal was analysed.

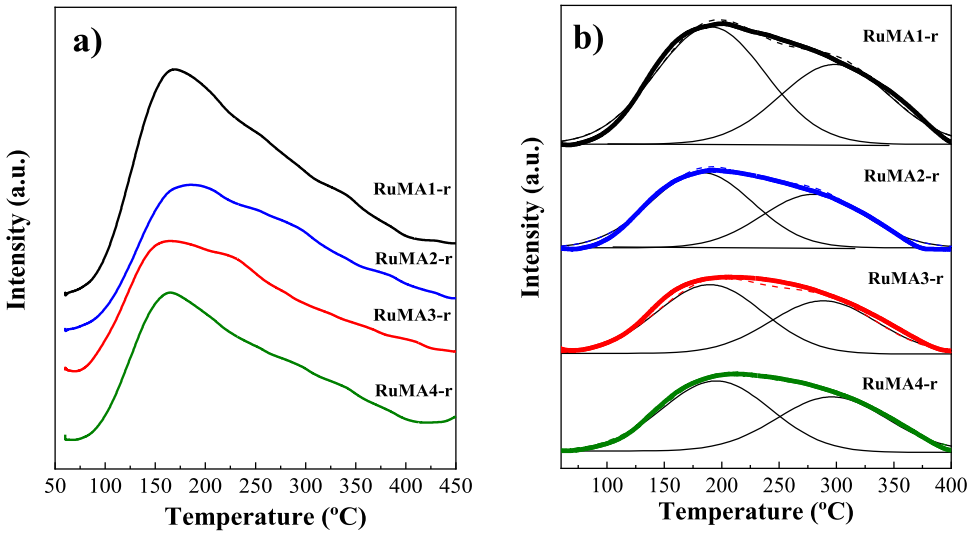

Fig. 6. (a) CO_2 and (b) NH_3 thermoprogrammed desorption for reduced catalysts.

The Al 2*s* signals in Fig. 7(a) for all samples presented a main broad peak at *ca.* 118.8 eV for RuMA1-r and RuMA2-r related to Al^{3+} [41], which indicates well-dispersed Al-O-Mg domains without phases segregation, as supported by XRD results [42,43]. A light shift to higher binding energy values was observed as the Mg/Al ratio increased, until 119.2 eV, supported the formation of $MgAl_2O_4$ spinel [44] that modifies Al electronic environment. Chloride presence was also confirmed (graph not shown) coming from the Ru salt precursor used for the catalysts' synthesis.

With respect to Mg 2*s* core level spectra in Fig. 7(b), the catalysts presented a broad peak that was deconvoluted into three contributions. The one between 86.8 and 87.3 eV is associated with magnesium oxide, obtained from the thermal treatment of the hydrotalcites [45]. That at 88.4 eV is assigned to $MgAl_2O_4$ spinel [44,46] and lastly the one at *ca.* 90.1 eV is attributed to superficial $Mg(OH)_2$ species [47]. In addition, given that mixed oxides derived from thermal treatment of hydrotalcites are prone to carbonation, specially MgO for its basic nature, the presence of $MgCO_3$ with a binding energy value close to 90.0 eV was also considered, since in the C 1*s* core level spectra (not shown) the presence of carbonates was evidenced [47]. Moreover, this deconvoluted signal's contribution was increased in samples with greater Mg/Al ratio.

The O 1*s* core level spectra for all reduced catalysts (Fig. 8(c)) were decomposed into three main contributions: at 529.8 eV attributed to lattice oxygen in metal oxides M-O; that at 531.1 eV due to $MgAl_2O_4$ and $Mg(OH)_2$ entities [44,47] and at *ca.* 532.2 eV, associated with carbonates from hydrotalcite [48]. Although the latter contribution is usually found at higher binding energy around 533 eV, water molecules could be crystallized and bonded to interlayered carbonate or hydroxyl groups through strong hydrogen bonds therefore decreasing the expected binding energy value, as previously reported by several authors [49–51]. Interestingly, it is observed that, as the Mg/Al molar ratio increases, so does the contribution of MgO phase, as observed from XRD patterns.

Lastly, for the Ru $3p_{3/2}$ core level spectra of fresh, reduced catalysts (Fig. 8(a)), all signals were deconvoluted into three contributions: the contribution at the lowest binding energy 460.8 eV is related to metallic Ru; the intermediate one at *ca.* 462.8 eV is associated with Ru (IV) oxide species and the one at highest binding energy of 464.5 eV is characteristic of oxychloride species from the metal precursor used for the synthesis and observed previously [52,53]. It is worth to mention the fact that the Ru^0 contribution decreased with the Mg/Al molar ratio in accordance with TPR results and CO chemisorption studies and, where a lower Ru^0 dispersion is observed at higher Mg/Al ratios.

In order to investigate potential changes in surface composition after

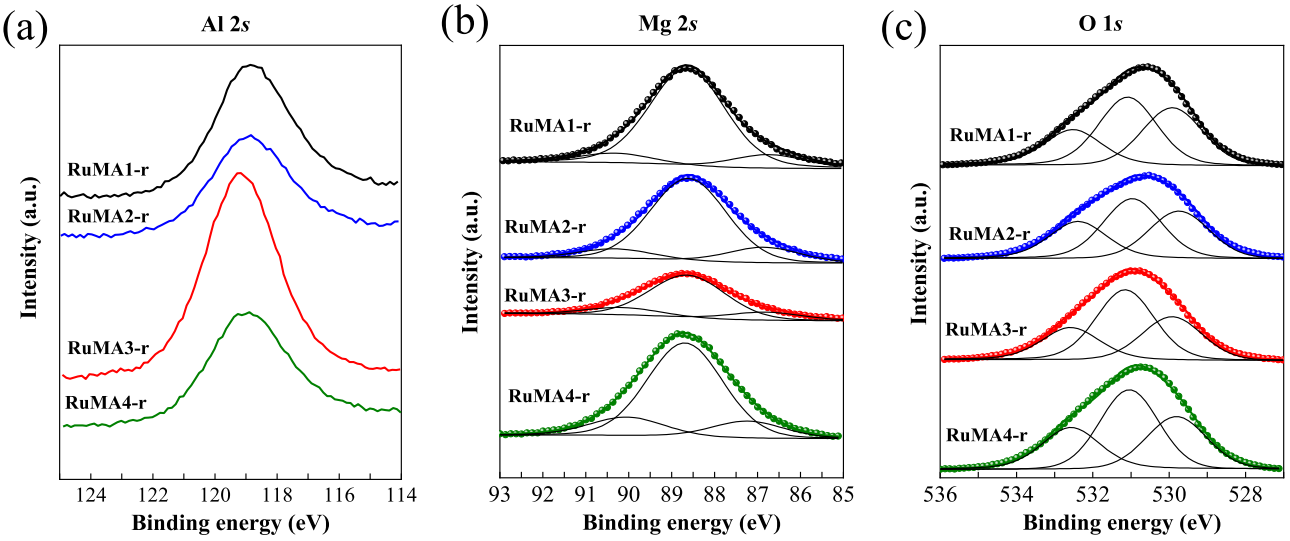

Fig. 7. (a) Al 2s, (b) Mg 2s and (c) O 1s core level spectra for reduced catalysts.

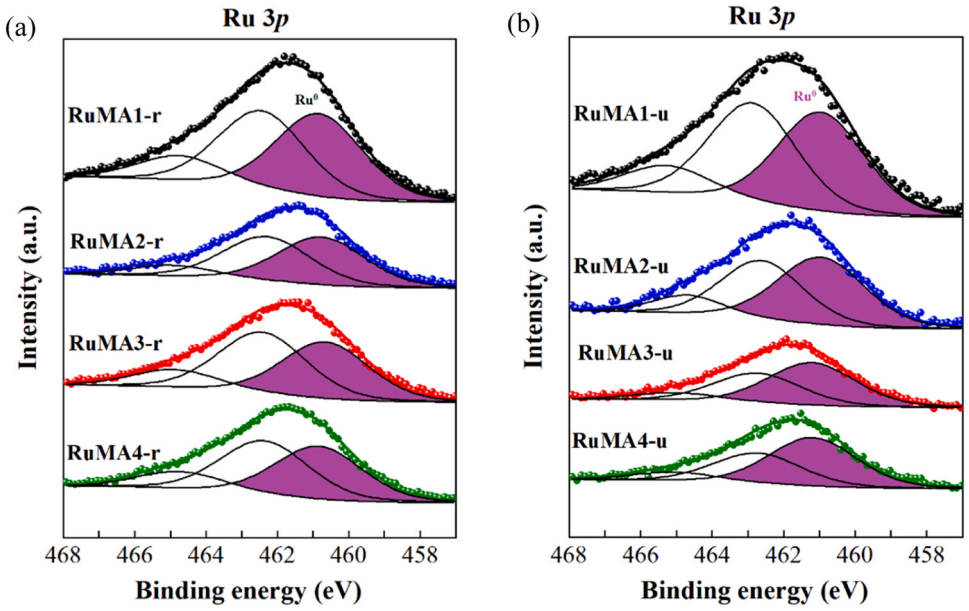

Fig. 8. Ru $3p_{3/2}$ core level spectra for reduced (a) and used (b) catalysts.

catalysis, XPS analysis of used catalysts were also carried out. Regarding the constituent elements of the supports, no significant changes were observed in the Al 2*s* signal (not shown), registering a main peak related to Al^{3+} species at 119 eV [41]. Mg 2*s* core level signals (not shown) did not change either showing the coexistence of MgO, $Mg(OH)_2$/$MgAl_2O_4$ and carbonates at binding energy values of 87.7, 88.4 and 88.8 eV,

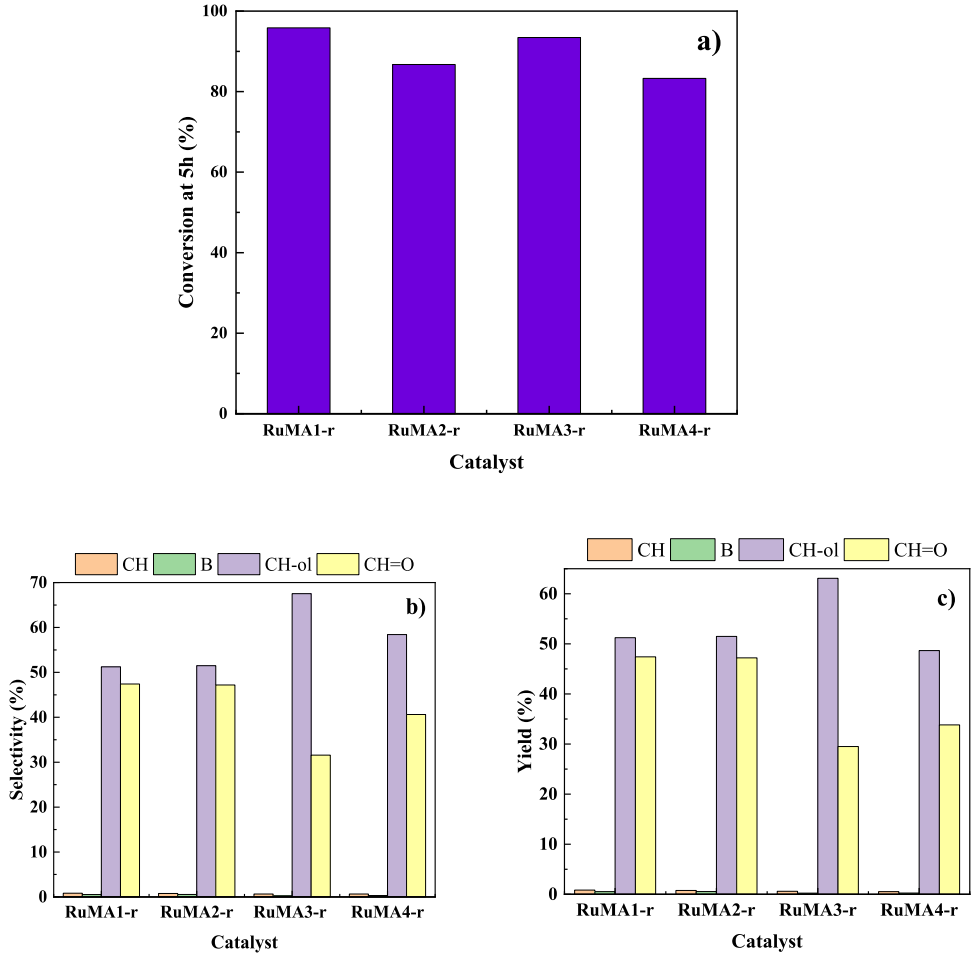

Fig. 9. (a) Conversion; (b) Selectivity to cyclohexane (CH), benzene (B), cyclohexanol (CH-ol) and cyclohexanone (CH═O); and (c) Yield to cyclohexane (CH), benzene (B), cyclohexanol (CH-ol) and cyclohexanone (CH═O) for all catalysts at 5 h of reaction.

respectively, as previously stated for reduced catalysts [46,47] and with similar proportion of each contribution. In line with this, O 1*s* core level spectra evidenced the same three contributions with minimal changes as for reduced samples. The Ru $3p_{3/2}$ core level signal in Fig. 8(b), showed the same three contributions but a greater contribution of metallic Ru (~ 461 eV) is observed in the samples with Mg/Al molar ratios 2, 3 and 4, as expected due to the reducing reaction environment. To note is that the RuMA1-r, which is the most active catalyst does not show this tendency, a similar spectrum is observed after testing, pointing to a great stability of Ru particle during testing.

3.2. Catalytic results

The reduced catalysts were tested in the selective hydrogenation of phenol at 30 bar and 200 °C to assess the influence of Mg/Al ratio on the catalytic performance, i.e., activity and selectivity. Fig. 9(a) displays the conversion at 5 h of reaction for all prepared catalysts, reaching conversion values higher than 80 % in all cases. The catalyst that achieved the highest conversion, 95.9 %, was RuMA1-r, suggesting that increasing the Mg/Al ratio may have a worsening effect on the catalytic activity. The ever-increasing tendency may be related to the hydrogen-rich environment activating Ru in the catalyst. As observed in Fig. 9(b), all the catalysts were selective to cyclohexanol and cyclohexanone as main reaction products, indicating that over these catalysts the reaction is likely to undergo via complete hydrogenation to form cyclohexanol, but also through a partial hydrogenation and further isomerization to give rise to cyclohexanone, as reported by other authors [5].

Liu et al. [55] studied phenol hydrogenation over Pd-Lewis acid catalyst, reporting that the reaction mechanism involved the cooperation of two activation works simultaneously: on the one hand, the activation of the hydrogen molecule on metallic active sites and, on the other hand, the eased attack of an incipient electrophile on one carbon of the benzene ring that became highly nucleophilic thanks to Lewis acid sites of the support. Moreover, in their work, the interaction of cyclohexane and $AlCl_3$ was studied by means of Fourier transform infrared spectroscopy, demonstrating that in the presence of Lewis acid sites the hydrogenation of cyclohexanone was suppressed. The selectivity towards cyclohexanol increased with Mg content, suggesting that the Mg content favoured the complete hydrogenation of the aromatic ring. This fact could be justified considering that Mg decreases the Lewis acidity of the support since this acidity is mainly due to aluminium sites [56], which are responsible for inhibiting complete hydrogenation, in fact, samples with lower Mg content, RuMA1-r and RuMA2-r, were the catalysts with the best selectivity to cyclohexanone, attaining values close to 45 %.

Thus, considering the product distribution in Fig. 9(b), the proposed reaction pathways are depicted in Fig. 10, and Table 3 collects the selectivities for each reaction route for all catalysts. It is observed that route 3 of hydrodeoxygenation is almost negligible in all catalysts, but not absent since cyclohexane and benzene were detected as products. In all case, route 2 involving the complete hydrogenation of the aromatic ring is preferred, especially in catalysts with high Mg content, which are the ones with the highest normalised acidity (see Table 2). The high selectivity to this reaction route could be explained considering that in acid sites, phenol is adsorbed in a co-planar configuration that ensures a strong interaction between the aromatic ring and the support [31], therefore favouring the complete hydrogenation to form cyclohexanol. On the other hand, route 1 is competitive with route 2 on catalysts with lower Mg content. In this route, the reaction mechanism involves a partial hydrogenation of the aromatic ring to form an enol intermediate that quickly isomerizes to form cyclohexanone [32]. The weaker interaction between the aromatic ring and the benzene ring in these samples favours the cyclohexanone desorption and therefore inhibits its subsequent hydrogenation.

Finally, reusability tests were carried out for the most active catalyst, RuMA1-r. After the reaction, the catalyst was dried and reduced before it was reused. The catalyst was tested for three runs. After each run, the reaction medium was removed, keeping the catalyst in the batch reactor, and adding a new feed solution. The conversions at 5 h for three cycles are plotted in Fig. 11. A decrease in the conversion value to 70.6 % was found in the first run, but the catalyst showed a good stability after 3 runs, as previously reported for RuRh-containing catalysts [54], and highlighting the stability of the monometallic catalysts prepared and studied in the present study.

The presented results evidence the important role of Mg/Al molar ratio present in the hydrotalcite in the properties of the resulting catalyst and, therefore, in the catalytic activity in the selective phenol hydrogenation. Although all samples were prepared following the same synthesis conditions, X-ray diffraction proved that RuMA1-c sample was the only one in which hydrotalcite phase was not detected after calcination, demonstrating that the lamellar structure of the hydrotalcite completely collapsed, while in the rest of the samples with greater Mg/Al ratio, some diffraction peaks related to hydrotalcite were present, which indicates that the Mg content had a great influence on the calcination

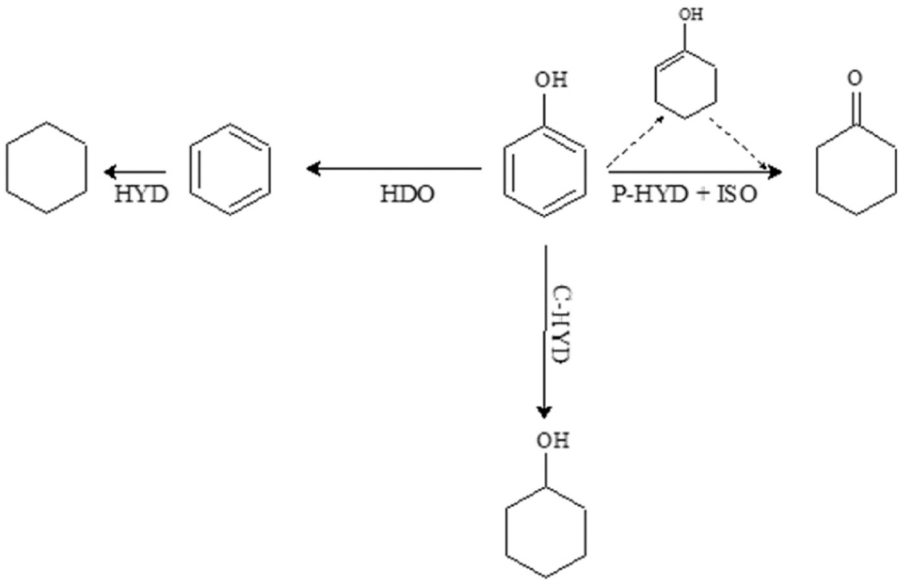

Fig. 10. Proposed reaction pathways based on products distribution.

Table 3
Catalysts selectivities to reaction routes.

Catalyst	Route 1 Partial hydrogenation + isomerization (P-HYD + ISO) (%)	Route 2 Complete hydrogenation (C-HYD) (%)	Route 3 Hydrodeoxygenation (HDO) (%)
RuMA1-r	47.4	51.2	1.4
RuMA2-r	47.2	51.5	1.3
RuMA3-r	31.6	67.6	0.8
RuMA4-r	40.6	58.4	1.0

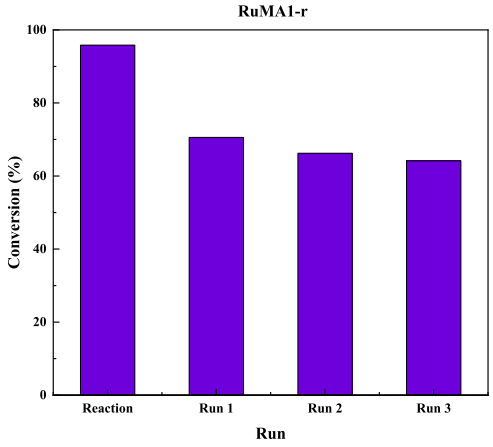

Fig. 11. Reutilization test for RuMA1-r catalyst.

temperature required to completely collapse the hydrotalcite to form the mixed oxides. Likewise, neither RuMA1-c nor RuMA1-r show any diffraction peaks related to $MgAl_2O_4$ spinel phase, even after the reduction process. As previously mentioned, spinel phases have been reported to be responsible for the decrease of the textural properties and in the availability of acid-base sites [35,37]. In fact, CO_2-TPD measurements pointed out that RuMA1-r was the sample with the highest basicity and acidity (the amount of adsorbed CO_2 and NH_3 per grams of sample, respectively), which progressively decreased with Mg content in the catalysts. Also, this sample contains the greatest proportion of Bronsted acid sites. Regarding the specific surface area, it was found that the increase of the Mg/Al molar ratio provoked a decrease in the specific surface area. RuMA1-c was the sample with the highest BET value which, taking into consideration the macroporous nature of the sample, could be related to the interparticle space in this sample. Since the RuMA1 sample was the one without presence of hydrotalcite nor $MgAl_2O_4$ spinel phase, Mg and Al was present as MgO and Al_2O_3, thus the porosity may be attributed to N_2 filling in the space between adjacent MgO and Al_2O_3 particles. On the contrary, in samples with Mg/Al molar ratio greater than 1, the formation of the spinel diminished the number of particles, which together with the increased crystallinity observed in XRD measurements, decreased the amount of N_2 that can condense in the interparticle space, which was reflected in BET values. With respect to the metallic dispersion, RuMA1-r catalyst again showed the greatest values. Lastly, the catalytic tests indicated that the RuMA1-r sample was the one with the highest conversion (95.9 %) and also the greatest selectivity to cyclohexanone (47.4 %). The higher specific surface area and the dispersion of the Ru active phase in the RuMA1-r catalyst and the absence of both hydrotalcite and $MgAl_2O_4$ spinel phase are responsible for the better catalytic performance on this catalyst in the selective hydrogenation of phenol.

4. Conclusions

In this work, a set of catalysts with 2 wt% ruthenium supported on mixed oxides derived from non-commercial hydrotalcites with different Mg/Al molar ratios (1, 2, 3 and 4) was synthesized. The catalytic test showed that the RuMA1-r catalyst was the most active catalyst attaining 95.9% conversion with 47.4 % selectivity to cyclohexanone, for which both the Mg/Al molar ratio and Ru are responsible. On the one hand, Mg/Al ratio was demonstrated to have an impact on the catalysis, which was supported by characterization results. A higher Mg loading gave rise to the formation of $MgAl_2O_4$ spinel phase, diminishing the specific surface area and the normalised acidity and basicity of the catalysts, as evidenced by N_2 physisorption and NH_3- and CO_2-TPD analyses, respectively. Moreover, samples with Mg/Al molar ratio over 1 also presented a hydrotalcite-like lamellar structure that suggested an incomplete collapse of the hydrotalcite after thermal treatment that governs the catalyst structure, Ru surface exposure, acidity and basicity and therefore the catalytic response of the prepared samples.

CRediT authorship contribution statement

Isabel Barroso Martín: Investigation, Writing – original draft, Validation. **Nadia Benmebirouk-Pareja:** Investigation, measurements. **Maia Montaña:** Investigation. **Juan Antonio Cecilia:** Investigation, experimental work, Writing – original draft, Writing – review & editing, Validation. **Antonia Infantes Molina:** Conceptualization, Validation, Supervision, Writing – original draft, Writing – review & editing, Funding acquisition. **Enrique Rodríguez-Castellón:** Investigation, Validation, Supervision, Writing – original draft, Writing – review & editing, Funding acquisition.

Declaration of Competing Interest

The authors declare the following financial interests/personal relationships which may be considered as potential competing interests: Enrique Rodriguez Castellon reports financial support was provided by Spain Ministry of Science and Innovation.

Data Availability

No data was used for the research described in the article.

Acknowledgments

This publication is part of the R&D project PID2021-126235OB-C32 funded by MCIN/ AEI/10.13039/501100011033/ and FEDER funds. . Funding for open access charge: Universidad de Málaga / CBUA. Funding for open access charge: Universidad de Málaga / CBUA is also acknowledged. IBM thanks University of Malaga for a postdoctoral grant.

References

[1] Q. Wu, L. Wang, B. Zhao, L. Huang, S. Yu, A.J. Ragauskas, Highly selective hydrogenation of phenol to cyclohexanone over a Pd-loaded N-doped carbon catalyst derived from chitosan, J. Colloid Interface Sci. 605 (2022) 82–90, https://doi.org/10.1016/J.JCIS.2021.07.077.
[2] M. Chatterjee, H. Kawanami, M. Sato, A. Chatterjee, T. Yokoyama, T. Suzuki, Hydrogenation of phenol in supercritical carbon dioxide catalyzed by palladium supported on Al-MCM-41: a facile route for one-pot cyclohexanone formation, Adv. Synth. Catal. 351 (2009) 1912–1924, https://doi.org/10.1002/ADSC.200900144.
[3] H. Zhang, S.M. Mahajani, M.M. Sharma, T. Sridhar, Hydration of cyclohexene with solid acid catalysts, Chem. Eng. Sci. 57 (2002) 315–322, https://doi.org/10.1016/S0009-2509(01)00375-X.

[4] H. Cheng, R. Liu, Q. Wang, C. Wu, Y. Yu, F. Zhao, Selective reduction of phenol derivatives to cyclohexanones in water under microwave irradiation, New J. Chem. 36 (2012) 1085–1090, https://doi.org/10.1039/C2NJ20990J.

[5] H. Chen, J. Sun, Selective hydrogenation of phenol for cyclohexanone: a review, J. Ind. Eng. Chem. 94 (2021) 78–91, https://doi.org/10.1016/J.JIEC.2020.11.022.

[6] Y. Wang, J. Zhang, X. Wang, M. Antonietti, H. Li, Boron- and fluorine-containing mesoporous carbon nitride polymers: metal-free catalysts for cyclohexane oxidation, Angew. Chem. Int. Ed. 49 (2010) 3356–3359, https://doi.org/10.1002/ANIE.201000120.

[7] N.H. Attanayake, M. Tang, Performance and pathways of electrochemical cyclohexane oxidation, Curr. Opin. Electrochem. 30 (2021), 100791, https://doi.org/10.1016/J.COELEC.2021.100791.

[8] U. Schuchardt, D. Cardoso, R. Sercheli, R. Pereira, R.S. Da Cruz, M.C. Guerreiro, D. Mandelli, E.V. Spinacé, E.L. Pires, Cyclohexane oxidation continues to be a challenge, Appl. Catal. A Gen. 211 (2001) 1–17, https://doi.org/10.1016/S0926-860X(01)00472-0.

[9] L.L.R. Vono, C. Broicher, K. Philippot, L.M. Rossi, Tuning the selectivity of phenol hydrogenation using Pd, Rh and Ru nanoparticles supported on ceria- and titania-modified silicas, Catal. Today 381 (2021) 126–132, https://doi.org/10.1016/J.CATTOD.2020.07.078.

[10] J.F. Zhu, G.H. Tao, H.Y. Liu, L. He, Q.H. Sun, H.C. Liu, Aqueous-phase selective hydrogenation of phenol to cyclohexanone over soluble Pd nanoparticles, Green Chem. 16 (2014) 2664–2669, https://doi.org/10.1039/C3GC42408A.

[11] B. Gao, J. Chen, Q. Zuo, H. Wang, W. Li, The critical role of Zr in controlling the activity of Pd/Beta on the hydrogenation of phenol to cyclohexanone, Chin. J. Chem. Eng. (2022), https://doi.org/10.1016/J.CJCHE.2022.07.033.

[12] A.N. Kay Lup, F. Abnisa, W.M.A.W. Daud, M.K. Aroua, Synergistic interaction of metal–acid sites for phenol hydrodeoxygenation over bifunctional Ag/TiO2 nanocatalyst, Chin. J. Chem. Eng. 27 (2019) 349–361, https://doi.org/10.1016/J.CJCHE.2018.08.028.

[13] M.J. Ndolomingo, N. Bingwa, R. Meijboom, Review of supported metal nanoparticles: synthesis methodologies, advantages and application as catalysts, J. Mater. Sci. 5515 (55) (2020) 6195–6241, https://doi.org/10.1007/S10853-020-04415-X.

[14] M. Monai, A.C. Banerjee, Catalyst-support interactions in heterogeneous catalysis: from fundamental concepts to applications, Catal. Today 382 (2021) 1–2, https://doi.org/10.1016/J.CATTOD.2021.09.021.

[15] G. Neri, A.M. Visco, A. Donato, C. Milone, M. Malentacchi, G. Gubitosa, Hydrogenation of phenol to cyclohexanone over palladium and alkali-doped palladium catalysts, Appl. Catal. A Gen. 110 (1994) 49–59, https://doi.org/10.1016/0926-860X(94)80104-5.

[16] N. Mahata, V. Vishwanathan, Gas phase hydrogenation of phenol over supported palladium catalysts, Catal. Today 49 (1999) 65–69, https://doi.org/10.1016/S0920-5861(98)00409-X.

[17] G. Xu, J. Guo, Y. Zhang, Y. Fu, J. Chen, L. Ma, Q. Guo, Selective hydrogenation of phenol to cyclohexanone over Pd–HAP catalyst in aqueous media, ChemCatChem 7 (2015) 2485–2492, https://doi.org/10.1002/CCTC.201500442.

[18] M. Li, Y. Li, L. Jia, Y. Wang, Tuning the selectivity of phenol hydrogenation on Pd/C with acid and basic media, Catal. Commun. 103 (2018) 88–91, https://doi.org/10.1016/J.CATCOM.2017.09.028.

[19] S. Scirè, S. Minicò, C. Crisafulli, Selective hydrogenation of phenol to cyclohexanone over supported Pd and Pd-Ca catalysts: an investigation on the influence of different supports and Pd precursors, Appl. Catal. A Gen. 235 (2002) 21–31, https://doi.org/10.1016/S0926-860X(02)00237-5.

[20] S. Narayanan, K. Krishna, Structure activity relationship in Pd/hydrotalcite: effect of calcination of hydrotalcite on palladium dispersion and phenol hydrogenation, Catal. Today 49 (1999) 57–63, https://doi.org/10.1016/S0920-5861(98)00408-8.

[21] J. Liu, H. Li, H. Li, Liquid-phase selective hydrogenation of phenol to cyclohexanone over Pd-Ce-B/hydrotalcite catalyst, Chin. J. Catal. 28 (2007) 312–316, https://doi.org/10.1016/S1872-2067(07)60029-1.

[22] A. Sreenavya, A. Sahu, A. Sakthivel, Hydrogenation of lignin-derived phenolic compound eugenol over ruthenium-containing nickel hydrotalcite-type materials, Ind. Eng. Chem. Res. 59 (2020) 11979–11990, https://doi.org/10.1021/ACS.IECR.0C01106/ASSET/IMAGES/LARGE/IE0C01106_0006.JPEG.

[23] K. Yan, Y. Liu, Y. Lu, J. Chai, L. Sun, Catalytic application of layered double hydroxide-derived catalysts for the conversion of biomass-derived molecules, Catal. Sci. Technol. 7 (2017) 1622–1645, https://doi.org/10.1039/C7CY00274B.

[24] Z. Bai, X. Chen, C. Li, W. Guan, P. Chen, C. Liang, Preparation of supported palladium catalyst from hydrotalcite-like compound for dicyclopentadiene resin hydrogenation, Mol. Catal. 484 (2020), 110728, https://doi.org/10.1016/J.MCAT.2019.110728.

[25] S. Narayanan, K. Krishna, Hydrotalcite-supported palladium catalysts: Part II. Preparation, characterization of hydrotalcites and palladium hydrotalcites for CO chemisorption and phenol hydrogenation, Appl. Catal. A Gen. 198 (2000) 13–21, https://doi.org/10.1016/S0926-860X(99)00496-2.

[26] Y. Yang, Z. Ren, S. Zhou, M. Wei, Perspectives on Multifunctional Catalysts Derived from Layered Double Hydroxides toward Upgrading Reactions of Biomass Resources, 2021. ⟨https://doi.org/10.1021/acscatal.1c00699⟩.

[27] S.D. Chaudhary, S.S. Rahatade, S.S. Joshi, N.A. Mali, Reduction of carbon dioxide to dimethylformamide using ruthenium doped Mg/Al hydrotalcites under supercritical conditions, J. CO_2 Util. 61 (2022), 102055, https://doi.org/10.1016/J.JCOU.2022.102055.

[28] D.P. Debecker, E.M. Gaigneaux, G. Busca, Exploring, tuning, and exploiting the basicity of hydrotalcites for applications in heterogeneous catalysis, Chem. - A Eur. J. 15 (2009) 3920–3935, https://doi.org/10.1002/CHEM.200900060.

[29] Y. Zhang, M. Liang, Y. Gan, O. Çopuroğlu, Effect of MgO content on the quantitative role of hydrotalcite-like phase in a cement-slag system during carbonation, Cem. Concr. Compos. 134 (2022), 104765, https://doi.org/10.1016/J.CEMCONCOMP.2022.104765.

[30] M. Thommes, K. Kaneko, A.V. Neimark, J.P. Olivier, F. Rodriguez-Reinoso, J. Rouquerol, K.S.W. Sing, IUPAC Technical Report Physisorption of Gases, with Special Reference to the Evaluation of Surface Area and Pore Size Distribution (IUPAC Technical Report), 2015. ⟨https://doi.org/10.1515/pac-2014-1117⟩.

[31] M. Faraldos, Técnicas de análisis y caracterización de materiales, 2a. edicio, Editorial CSIC Consejo Superior de Investigaciones Científicas, Madrid, 2011.

[32] H. Armendáriz, A. Guzmán, J.A. Toledo, M.E. Llanos, A. Vázquez, G. Aguilar-Ríos, Isopentane dehydrogenation on Pt-Sn catalysts supported on Al-Mg-O mixed oxides: effect of Al/Mg atomic ratio, Appl. Catal. A Gen. 211 (2001) 69–80, https://doi.org/10.1016/S0926-860X(00)00836-X.

[33] A. Ballarini, P. Benito, G. Fornasari, O. Scelza, A. Vaccari, Role of the composition and preparation method in the activity of hydrotalcite-derived Ru catalysts in the catalytic partial oxidation of methane, Int. J. Hydrog. Energy 38 (2013) 15128–15139, https://doi.org/10.1016/J.IJHYDENE.2013.08.135.

[34] L.S. Carvalho, A.R. Martins, P. Reyes, M. Oportus, A. Albonoz, V. Vicentini, M. do, C. Rangel, Preparation and characterization of Ru/MgO-Al2O3 catalysts for methane steam reforming, Catal. Today 142 (2009) 52–60, https://doi.org/10.1016/J.CATTOD.2009.01.010.

[35] J. Song, S. Wang, Y. Xu, Q. Liu, Y. Zhao, LDH derived MgAl2O4 spinel supported Pd catalyst for the low-temperature methane combustion: roles of interaction between spinel and PdO, Appl. Catal. A Gen. 621 (2021), 118211, https://doi.org/10.1016/J.APCATA.2021.118211.

[36] P. Kuśtrowski, D. Sułkowska, L. Chmielarz, A. Rafalska-Łasocha, B. Dudek, R. Dziembaj, Influence of thermal treatment conditions on the activity of hydrotalcite-derived Mg–Al oxides in the aldol condensation of acetone, Microporous Mesoporous Mater. 78 (2005) 11–22, https://doi.org/10.1016/J.MICROMESO.2004.09.011.

[37] S.J. Park, S.H. Kang, H.K. Min, Y.H. Choi, J.W. Lee, Depolymerization of polystyrene over Mgx-Aly-O catalysts derived from hydrotalcites: effect of Mg/Al ratio on the basicity and catalytic performance, Mol. Catal. 506 (2021), 111546, https://doi.org/10.1016/J.MCAT.2021.111546.

[38] P. Kuśtrowski, L. Chmielarz, E. Bozek, M. Sawalha, F. Roessner, Acidity and basicity of hydrotalcite derived mixed Mg–Al oxides studied by test reaction of MBOH conversion and temperature programmed desorption of NH3 and CO_2, Mater. Res. Bull. 39 (2004) 263–281, https://doi.org/10.1016/J.MATERRESBULL.2003.09.032.

[39] W. Zhao, R. Wang, Y. Wang, J. Feng, C. Li, G. Chen, Effect of LDH composition on the catalytic activity of Ru/LDH for the hydrolytic dehydrogenation of ammonia borane, Int. J. Hydrog. Energy 44 (2019) 14820–14830, https://doi.org/10.1016/J.IJHYDENE.2019.04.052.

[40] J.I. Di Cosimo, C.R. Apesteguía, M.J.L. Ginés, E. Iglesia, Structural requirements and reaction pathways in condensation reactions of alcohols on MgyAlOx catalysts, J. Catal. 190 (2000) 261–275, https://doi.org/10.1006/JCAT.1999.2734.

[41] R. Prakash, S. Kumar, V. Kumar, R.J. Choudhary, D.M. Phase, Optical and x-ray photoelectron spectroscopy studies of α-Al2O3, AIP Conf. Proc. 1731 (2016), 050097, https://doi.org/10.1063/1.4947751.

[42] N. Pino, G. Hincapié, D. López, Hydrodeoxygenation of furfuryl alcohol over Cu/MgAl and Cu/ZnAl catalysts derived from hydrotalcite-like precursors, Ing. Invest. 37 (2017) 34–42, https://doi.org/10.15446/ing.investig.v37n1.57991.

[43] G. Hincapié, D. López, A. Moreno, Infrared analysis of methanol adsorption on mixed oxides derived from Mg/Al hydrotalcite catalysts for transesterification reactions, Catal. Today 302 (2018) 277–285, https://doi.org/10.1016/J.CATTOD.2017.05.052.

[44] B.R. Strohmeier, Magnesium aluminate (MgAl2O4) by XPS, Surf. Sci. Spectra 3 (1994) 121–127, https://doi.org/10.1116/1.1247772.

[45] J.J. Creasey, A. Chieregato, J.C. Manayil, C.M.A. Parlett, K. Wilson, A.F. Lee, Alkali- and nitrate-free synthesis of highly active Mg–Al hydrotalcite-coated alumina for FAME production, Catal. Sci. Technol. 4 (2014) 861–870, https://doi.org/10.1039/C3CY00902E.

[46] B.R. Strohmeier, Magnesium aluminate (MgAl2O4) by XPS, Surf. Sci. Spectra 3 (2021) 121, https://doi.org/10.1116/1.1247772.

[47] A. Le Febvrier, J. Jensen, P. Eklund, Wet-cleaning of MgO(001): modification of surface chemistry and effects on thin film growth investigated by x-ray photoelectron spectroscopy and time-of-flight secondary ion mass spectroscopy, J. Vac. Sci. Technol. A Vac. Surf. Films 35 (2017), 021407, https://doi.org/10.1116/1.4975595.

[48] J. Chen, Y. Song, D. Shan, E.H. Han, In situ growth of Mg–Al hydrotalcite conversion film on AZ31 magnesium alloy, Corros. Sci. 53 (2011) 3281–3288, https://doi.org/10.1016/J.CORSCI.2011.06.003.

[49] M. Mora, M.I. López, C. Jiménez-Sanchidrián, J.R. Ruiz, MIR and NIR spectroscopy of sol-gel hydrotalcites with various trivalent cations, J. Sol-Gel Sci. Technol. 55 (2010) 59–65, https://doi.org/10.1007/S10971-010-2213-X/FIGURES/7.

[50] F. Millange, R.I. Walton, D. O'Hare, Time-resolved in situ X-ray diffraction study of the liquid-phase reconstruction of Mg–Al–carbonate hydrotalcite-like compounds, J. Mater. Chem. 10 (2000) 1713–1720, https://doi.org/10.1039/B002827O.

[51] M.A. Aramendía, V. Borau, C. Jiménez, J.M. Marinas, J.R. Ruiz, F.J. Urbano, Comparative study of Mg/M(III) (M = Al, Ga, In) layered double hydroxides obtained by coprecipitation and the sol–gel method, J. Solid State Chem. 168 (2002) 156–161, https://doi.org/10.1006/JSSC.2002.9655.

[52] D.J. Morgan, Resolving ruthenium: XPS studies of common ruthenium materials, Surf. Interface Anal. 47 (2015) 1072–1079, https://doi.org/10.1002/SIA.5852.

[53] P. Braos-García, C. García-Sancho, A. Infantes-Molina, E. Rodríguez-Castellón, A. Jiménez-López, Bimetallic Ru/Ni supported catalysts for the gas phase hydrogenation of acetonitrile, Appl. Catal. A Gen. 381 (2010) 132–144, https://doi.org/10.1016/J.APCATA.2010.03.061.

[54] W. Jiang, J.-P. Cao, C. Zhang, W. Tang, C.-X. Chen, Z.-M. He, X.-Y. Zhao, H.-C. Bai, Highly efficient hydrogenation of phenol and lignin-derived compounds over Ru-Rh bimetallic nanoparticles supported on α-Al2O3 at room temperature, Fuel 351 (2023), 128859, https://doi.org/10.1016/J.FUEL.2023.128859.

[55] H. Liu, T. Jiang, B. Han, S. Liang, Y. Zhou, Selective phenol hydrogenation to cyclohexanone over a dual supported Pd-Lewis acid catalyst, Science 326 (80) (2009) 1250–1252, https://doi.org/10.1126/SCIENCE.1179713/SUPPL_FILE/LIU.SOM.PDF.

[56] A.A. Vargas-Tah, R.C. García, L.F.P. Archila, J.R. Solis, A.J.G. López, A study on sulfur reduction in FCC gasoline using Zn-Mg-Al spinels, Catal. Today 107–108 (2005) 713–718, https://doi.org/10.1016/J.CATTOD.2005.07.001.